International Journal of Heat and Mass Transfer 52 (2009) 3334–3340

Contents lists available at ScienceDirect

International Journal of Heat and Mass Transfer

journal homepage: www.elsevier.com/locate/ijhmt

Inverse prediction of wall temperature distribution on a cylinder exposed to radiatively active flow

Sang Heon Han *, Seung Wook Baek, Ju Hyeong Cho

Department of Aerospace Engineering, Korea Advanced Institute of Science and Technology, 373-1 Guseong-dong, Yuseong-gu, Daejeon 305-701, Republic of Korea

ARTICLE INFO

Article history:
Received 9 April 2008
Received in revised form 12 September 2008
Available online 14 March 2009

Keywords:
Inverse analysis
Conjugate gradient method
Radiation
Heat exchanger

ABSTRACT

In this study, the unknown wall temperature profile of a cylinder was predicted by applying the inverse method. The temperature profile of the cylinder wall was predicted from the given temperature data at measurement points near the cylinder wall. The cylinder was assumed to represent a typical pipe in a bundle of heat exchange tubes operating in a high temperature system. Radiative heat transfer was incorporated as one of major heat transfer modes to consider a hot gas flow passing over the cylinder. The corresponding inverse problem was solved by minimizing an objective function by applying the iterative conjugate gradient method. A multi-block grid composed of three different blocks was used for better computational accuracy and convenience in locating the measurement points. A new method, which could be applicable to non-symmetric geometry, was adopted to solve the adjoint equation. In this study, the effects of number and location of the measurement points were numerically investigated. When the measurement points were too close to the cylinder, the predicted temperature profile exhibited larger fluctuations. The results have also shown that an appropriate number of measurement points were required to improve the prediction of the boundary temperature profile.

1. Introduction

Heat exchangers [1] have been widely used in various engineering applications such as chip-cooling, refrigerating, power production, waste heat recovery, and chemical processing. They can operate either in moderate temperature conditions [2] or in high temperature conditions [3]. Chip-cooling or refrigerating systems employ heat exchangers operating in the moderate temperature regime, in which conduction and convection are the major heat transfer mechanisms. On the other hand, heat exchangers built in energy consuming devices, such as dryers, ovens, and furnaces, are exposed to a high temperature environment, in which an additional heat transfer mechanism, namely radiation, becomes operative.

Inverse analysis is well suited for the problem of finding out unknown input conditions corresponding to the given measurement data. There have been a number of efforts to develop efficient inverse methods and their application to practical situations. For example, the prediction of the outer wall temperature profile of a target pipe in a heat exchanger tube bundle can be enabled by an inverse analysis technique. Then, such a temperature profile can be used in the evaluation of the corresponding tube wall heat flux to design an improved heat exchanger. In practice, the inverse heat conduction techniques have been utilized to reduce experimental burdens by the prediction of accurate heat transfer rates in many heat conduction problems. However, the inverse heat transfer analysis has been applied mainly to conduction and convection problems, while its applications to the inverse radiation problem have been quite limited.

Liu et al. [4] studied a one-dimensional radiation problem to estimate the temperature and wall emissivity simultaneously. Li [5] estimated the radiative properties while considering both conduction and radiation heat transfers using the conjugate gradient method (CGM). Kim and Charette [6] predicted optical properties by using the CGM with the known boundary radiation intensity. They attempted to apply the inverse technique to medical devices that capture images of the human body with the aim of finding diseases in tissues. Hong and Baek [7] attempted to determine the inlet temperature profile for two-phase laminar flow in a channel including radiation effect by using the CGM as an inverse algorithm. They also considered inverse radiation in the recent work dealing with natural convection [8].

The actual applications of inverse analysis to heat exchanger systems are quite few. Szczygiel and Fic [9] estimated the inlet boundary velocity corresponding to the given temperature measurement data in a heat exchanger system. They adopted the potential function for flow calculation and method to inversely obtain the inlet velocity. Huang et al. [10] calculated the heat transfer coefficients for a plate-tube heat exchanger using the steepest descent method (SDM). Chen and Yang [11] applied an inverse technique to predict the heat transfer rate around two in-line

* Corresponding author. Tel.: +82 42 869 3714; fax: +82 42 869 3710.
E-mail address: freezia@kaist.ac.kr (S.H. Han).

0017-9310/$ - see front matter © 2009 Elsevier Ltd. All rights reserved.
doi:10.1016/j.ijheatmasstransfer.2008.09.044

Nomenclature

Roman symbols

c_p	specific heat of gas (J/(kg K))
d	distance of measurement points from cylinder wall
d^k	direction of descent
D	diameter of cylinder
F	boundary temperature of inner cylinder wall
H,L	height and width of domain
I	radiation intensity
k_g	conductivity of gas (W/(m K))
M	number of measurement points
$\vec{n}$	unit normal vector
N	radiation strength parameter
p	pressure
Pe	Peclet number
Re	Reynolds number
$\vec{q}^R$	radiative heat flux vector
s	path of cylinder wall
$\vec{s}$	unit direction vector
S	objective function
T	temperature
u,v	velocity components in x and y directions
x,y	coordinates
Y_m	temperature at the measurement points

Greek symbols

α	absorption coefficient
ρ	density of gas (kg/m^3)
θ	angular variation (degree)
λ_T,λ_R	Lagrange multipliers
β^k	search step
γ^k	conjugate coefficient
σ	deviation of measurement
σ_{AB}	Stefan–Boltzmann constant, = $5.67 \times 10^{-8}(W/(m^2 \cdot K^4))$
Ω	solid angle (sr)

Superscripts

$*$	primitive dimensional variable
k	iteration step

Subscripts

b	boundary
g	gas
i	inflow
m	measurement

cylinders with the CGM. However, radiation heat transfer to the heat exchange pipes was not considered by them.

In this study, an inverse approach is presented to predict the outer wall temperature profile of a cylinder, which represents a single pipe in a heat exchanger tube bundle. The conjugate gradient method (CGM) is used as the inverse algorithm that transpired to produce a stable solution for unstable inverse problems. It is assumed that the cylinder is exposed to a high temperature gas flow, which involves radiation heat transfer by absorption and emission. Heat transfer from the hot gas into the cylinder is dependent on radiation as well as conduction and convection. Further to the conductive and convective disturbances arising from the boundary temperature perturbation, the radiative disturbances have also been taken into account to calculate the adjoint equation in the CGM.

2. Formulation

2.1. Direct problem

Fig. 1 shows a schematics of two neighboring cylinders in a tube bundle under a hot gas flow. The angle (θ) is introduced to describe a boundary wall temperature profile on the cylinder, which may be uniform or variant with θ. All the measurement points are located along the circular line around the cylinder whose center coincides with that of the cylinder.

The steady continuity, laminar Navier–Stokes equations, and energy equation with a constant density can be described in the Cartesian coordinate as follows:

$$\frac{\partial u}{\partial x}+\frac{\partial v}{\partial y}=0 \tag{1}$$

$$u\frac{\partial u}{\partial x}+v\frac{\partial u}{\partial y}=-\frac{\partial p}{\partial x}+\frac{1}{\mathrm{Re}}\left(\frac{\partial^2 u}{\partial x^2}+\frac{\partial^2 u}{\partial y^2}\right) \tag{2}$$

$$u\frac{\partial v}{\partial x}+v\frac{\partial v}{\partial y}=-\frac{\partial p}{\partial y}+\frac{1}{\mathrm{Re}}\left(\frac{\partial^2 v}{\partial x^2}+\frac{\partial^2 v}{\partial y^2}\right) \tag{3}$$

$$u\frac{\partial T}{\partial x}+v\frac{\partial T}{\partial y}=\frac{1}{Pe}\left(\frac{\partial^2 T}{\partial x^2}+\frac{\partial^2 T}{\partial y^2}\right)-\frac{1}{Pe}\nabla\cdot\vec{q}^R \tag{4}$$

The radiant intensity for a gray medium along a path $\vec{s}$ through a non-scattering medium is given by:

$$\frac{dI(\vec{s})}{ds}=\alpha I_b-\alpha I(\vec{s}) \tag{5}$$

The effect of radiation in energy equation is expressed in the form of divergence of radiative heat flux.

$$\nabla\cdot\vec{q}^R=\frac{\alpha}{N}\left(T^4-\frac{1}{4}\int I(\vec{s})d\Omega\right) \tag{6}$$

Above all equations are non-dimensional forms of ordinary governing equations with the following non-dimensional variables.

$$x=\frac{x^*}{D^*},\quad y=\frac{y^*}{D^*},\quad T=\frac{T^*}{T_i^*},\quad u=\frac{u^*}{u_i^*},\quad v=\frac{v^*}{u_i^*},$$
$$p=\frac{p^*}{\rho u_i^{*2}},\quad \mathrm{Re}=\frac{\rho u_i^* D^*}{\mu},\quad Pe=\frac{\rho c_p D^* u_i^*}{k_g},\quad I=\frac{I^*}{\sigma_{SB}T_i^{*4}},$$
$$s=D^*s^*,\quad \alpha=D^*\alpha^*,\quad N=\frac{k_g\alpha^*}{4\sigma_{SB}T_i^{*3}} \tag{7}$$

Here, superscript $*$ denotes primitive variable. u_i^* and T_i^* are inflow values of velocity and temperature. D^* is the cylinder diameter used for the characteristic length. I^*, s^*, α^* are the radiation intensity, a path of intensity, absorption coefficient, respectively. Re, Pe, α, and N are the resulting dimensionless parameters.

Temperature and velocity are specified on the wall boundaries while the normal gradients of all the variables are set to zero on the symmetric boundary.

$$\textit{inlet}: \quad u=1,\quad v=0,\quad T=1 \tag{8a}$$

$$\textit{outlet and symmetry}: \quad \frac{\partial u}{\partial n}=\frac{\partial v}{\partial n}=\frac{\partial T}{\partial n}=0 \tag{8b}$$

$$\textit{cylinder wall}: \quad u=v=0,\quad T=F(x,y)=F(\theta) \tag{8c}$$

Boundary conditions for intensity are described in the following equations where subscript b denotes boundary.

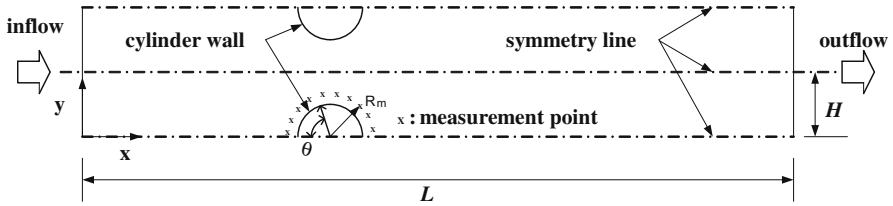

Fig. 1. Schematics of two neighboring cylinders.

$$\textit{symmetry}: \quad \frac{\partial I}{\partial n} = 0 \tag{9a}$$

$$\textit{others}: \quad I(\vec{s}) = \frac{\varepsilon_b}{\pi} T_b^4 + \frac{(1-\varepsilon_b)}{\pi} \int_{\vec{n}\cdot\vec{s}'<0} |\vec{n}\cdot\vec{s}'| I(\vec{s}') d\Omega' \tag{9b}$$

ε_b is the boundary emissivity and $\vec{n}$ is the unit normal vector to the boundary.

2.2. Inverse problem

The cylinder wall temperature is assumed unknown and is to be predicted by using the inverse technique. The unknown temperature distribution $F(\theta)$ around the cylinder wall is acquired by minimizing the objective function as follows:

$$S(F(\theta)) = \sum_{m=1}^{M} [Y_m(x,y) - T_g(x_m, y_m; F(\theta))]^2 \tag{10}$$

where Y_m and T_g denote measured temperature and predicted temperature at the sensor locations. M is the total number of probes. The calculated temperature T_g is obtained by solving the direct problem with $F(\theta)$.

2.2.1. Sensitivity problem

Before proceeding with the sensitivity problem, a representative variable ϕ is introduced, which can be one of the variables involved such as T or I. The sensitivity problem can be obtained by assuming that ϕ is perturbed by an amount of $\Delta\phi$, when $F(\theta)$ is perturbed by $\Delta F(\theta)$. Then, by replacing ϕ with $\phi + \Delta\phi$ and $F(\theta)$ with $F(\theta) + \Delta F(\theta)$ in all the equations of direct problem and subtracting the original direct problem from the resulting expressions, the following sensitivity equations are obtained:

$$u\frac{\partial \Delta T}{\partial x} + v\frac{\partial \Delta T}{\partial y} = \frac{1}{Pe}\left(\frac{\partial^2 \Delta T}{\partial x^2} + \frac{\partial^2 \Delta T}{\partial y^2}\right) - \frac{1}{Pe}\frac{\alpha}{N}\left(4T^3\Delta T - \frac{1}{4}\int \Delta I d\Omega\right) \tag{11}$$

$$\frac{d\Delta I(\vec{s})}{ds} = \frac{4\alpha}{\pi} T^3 \Delta T - \alpha \Delta I(\vec{s}) \tag{12}$$

The boundary conditions for temperature and velocity described in Eq. (8) are transformed into the following equations.

$$\textit{inlet}: \quad \Delta T = 0 \tag{13a}$$

$$\textit{outlet and symmetry}: \quad \frac{\partial \Delta T}{\partial n} = 0 \tag{13b}$$

$$\textit{cylinder wall}: \quad \Delta T = \Delta F \tag{13c}$$

Transformations are also performed for the boundary conditions of intensity described in Eq. (9).

$$\textit{symmetry}: \quad \frac{\partial \Delta I}{\partial n} = 0 \tag{14a}$$

$$\textit{others}: \quad \Delta I(\vec{s}) = \frac{4\varepsilon_b}{\pi} T_b^3 \Delta T_b + \frac{(1-\varepsilon_b)}{\pi} \int_{\vec{n}\cdot\vec{s}'<0} |\vec{n}\cdot\vec{s}'| \Delta I(\vec{s}') d\Omega' \tag{14b}$$

2.2.2. Adjoint problem

To derive the adjoint problem, two Lagrange multipliers, $\lambda_T(x,y)$ and $\lambda_R(x,y)$, are introduced. Two governing equations for temperature and intensity are multiplied by the above multipliers. Each resulting expression is integrated over the space domain, and added to the right-hand side of the objective function to yield:

$$\begin{aligned} S(F(\theta)) = {} & \sum_{m=1}^{M} [Y_m(x,y) - T_g(x_m, y_m; F(\theta))]^2 \\ & - \int_x \int_y \lambda_T(x,y) \left[u\frac{\partial T}{\partial x} + v\frac{\partial T}{\partial y} - \frac{1}{Pe}\left(\frac{\partial^2 T}{\partial x^2} + \frac{\partial^2 T}{\partial y^2}\right) + \frac{1}{Pe}\nabla\cdot\vec{q}^R \right] dxdy \\ & - \int_x \int_y \int_\Omega \lambda_R(x,y,\Omega) \left[\frac{dI(\vec{s})}{ds} - \alpha I_b + \alpha I(\vec{s}) \right] d\Omega dxdy \end{aligned} \tag{15}$$

Next, the variation $\Delta S(F(\theta))$ is derived. After some algebraic manipulations, the resulting equations are compelled to be zero. Then, the following adjoint problem is obtained to yield the governing equations for the Lagrange multipliers.

$$u\frac{\partial \lambda_T}{\partial x} + v\frac{\partial \lambda_T}{\partial y} = -\frac{1}{Pe}\left(\frac{\partial^2 \lambda_T}{\partial x^2} + \frac{\partial^2 \lambda_T}{\partial y^2}\right) + \frac{1}{Pe}\frac{4\alpha}{N}T^3\lambda_T - \frac{1}{Pe}\frac{4}{\pi}T^3\int_\Omega \lambda_R d\Omega + \frac{1}{Pe}\sum_{m=1}^{M} 2[Y_m - T_g]\delta(x-x_m)\delta(y-y_m) \tag{16}$$

$$\frac{d\lambda_R(\vec{s})}{ds} = -\frac{\alpha}{4N}\lambda_T + \lambda_R(\vec{s}) \tag{17}$$

where δ is the Dirac delta function. The boundary conditions for two Lagrange multipliers are described in the following equations.

$$\textit{symmetry}: \quad \frac{\partial \lambda_T}{\partial n} = \frac{\partial \lambda_R}{\partial n} = 0 \tag{18a}$$

$$\textit{outlet}: \quad \frac{\partial \lambda_T}{\partial n} = 0, \quad \lambda_R = 0 \tag{18b}$$

$$\textit{others}: \quad \lambda_T = \lambda_R = 0 \tag{18c}$$

Finally, the gradient direction of the objective function is determined by:

$$\nabla S[F(\theta)] = \frac{DS}{DF} = \left.\frac{\partial \lambda_T}{\partial n}\right|_{\textit{cylinder wall}} \tag{19}$$

2.2.3. Iterative procedure

The current kth iteration proceeds with the known values of ϕ, $\Delta\phi$, $\lambda_T(x,y)$,$\lambda_R(x,y)$, and $\nabla S(F(\theta))$ which are available from the previous $(k-1)$th iteration step. The boundary temperature at the $(k+1)$th step is computed from:

$$F^{k+1}(\theta) = F^k(\theta) - \beta^k d^k(\theta) \tag{20}$$

Here d^k is the direction of descent which is defined as:

$$d^k = \nabla S[F^k(\theta)] + \gamma^k d^{k-1} \tag{21}$$

where γ^k can be calculated from the Fletcher–Reeves expression [12] as follows:

$$\gamma^k = \frac{\int_{\textit{cylinder}} \{\nabla S[F^k(\theta)]\}^2 ds}{\int_{\textit{cylinder}} \{\nabla S[F^{k-1}(\theta)]\}^2 ds} \quad \text{with } \gamma^0 = 0 \tag{22}$$

The search step size β^k is determined by minimizing the functional $S(F^{k+1}(\theta))$ defined in Eq. (10) with respect to β^k as follows:

$$\beta^k = \frac{\sum_{m=1}^{M} [T_g(x_m, y_m; F^k(\theta)) - Y_m] \Delta T_g(x_m, y_m; d^k)}{\sum_{m=1}^{M} [\Delta T_g(x_m, y_m; d^k)]^2} \tag{23}$$

Here $\Delta T_g(x_m,y_m;d^k)$ is the solution of the sensitivity problem which is calculated by setting $\Delta F(\theta) = d^k$.

2.2.4. Discrepancy principle for stopping criterion

The iteration process reaches convergence if the objective functional $S(F^{k+1}(\theta))$ is reduced to a value smaller than tolerance ε.

$$S(P^{k+1}) < \varepsilon \tag{24}$$

As the estimated temperatures approach the measured temperatures that are liable to inherently contain some error, a large oscillation may appear during the minimization of the objective functional. However, the CGM used to produce smooth solutions if the discrepancy principle is used as stopping criterion. When the residuals between measured and estimated temperature are of the same order magnitude as σ

$$|Y(x_{measured}, y_{measured}) - T(x_{estimated}, y_{estimated})| \approx \sigma \tag{25}$$

where σ is the standard deviation of the measurement which is assumed to be a constant. The following expression is obtained for stopping criterion by substituting Eq. (25) into Eq. (10):

$$\varepsilon = \sum_{m=1}^{M} \sigma^2 = M\sigma^2 \tag{26}$$

Finally, the stopping criterion is given by Eq. (24) with ε determined from Eq. (26).

3. Numerical method

A multi-block grid has been adopted for two reasons. The first is to obtain a more favorable grid in the region around the cylinder, which belongs to the area of most concern in the calculation domain. The second is to set the measurement points at an equal distance from the cylinder wall. CAFA code [13] has been modified to use multi-block grids. The finite-volume method for radiation (FVM) has been used for prediction of radiation [14–17]. The FVM for radiation is a flux type of method similar to the discrete ordinates method (DOM). As a geometrical space is discretized into a finite number of control volumes, angular direction is also discretized into a finite number of control angles. The inflow and outflow of radiant energy across control volume faces are balanced with attenuation and augmentation of radiant energy within each control volume and each control angle.

Adjoint equations are slightly different from the original conserved equations. The first derivative terms have changed to negative terms in the process of deriving the adjoint equations as shown in Eqs. (16) and (17). The coordinate transformation [7,8] is applied to express the adjoint equations in the same form as the original conserved equations. The convective term in Eq. (16) and first spatial derivative term in Eq. (17) can be transformed to have a positive sign by replacing x with $L - x$ and y with $H - y$. But some difficulties still exist in applying discretization of the transformed equations to the present geometry because it is not symmetric with respect to y-axis. It is necessary to devise a method with which the coordinate transformed equation can be solved in non-symmetric geometry.

When discretization of λ_T is performed on the resulting coordinate transformed equations, the mirrored coordinate, as shown in Fig. 2, is used. The figure depicts that the positions of four neighboring cells are interchanged by mirroring. But discretization of the diffusion term does not change with the interchange of four neighboring cells. This is because the direction is irrelevant to the diffusion term. However, the convective term is changed, because it depends on direction. If u_E is positive, the point E becomes

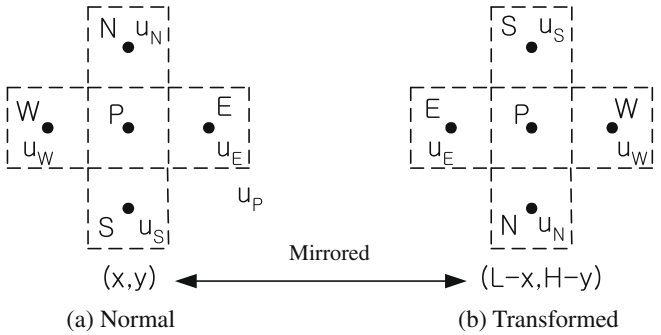

Fig. 2. Mirroring of four neighboring cells by coordinate transformation.

downstream to the point P by the interchange, and vice versa. A reverse concept for normal convection occurs in discretizing λ_T with the mirrored coordinate. If this reversed convection concept is applied to discretization of the transformed equation, the discretization can be successfully preformed without the mirrored coordinate. The same procedure is used for discretization of λ_R because the FVM for radiation uses the upwind concept to treat incoming radiation. So an outgoing ray of λ_R is considered to be an incoming one in the reversed convection concept.

4. Results and discussion

4.1. Direct problem calculation

Since the problem is symmetric with respect to the center line depicted in Fig. 1, only a half section of the depicted domain is solved. The cylinder diameter D and domain height H have the same value of 1.0 and the domain length L is 12. Fig. 3(a) shows the computational grid, which is composed of three different structured blocks corresponding to the upstream, near-cylinder and downstream regions. The grid sizes for these three blocks are 31×26, 91×29, and 101×26, respectively. The gird is clustered around the cylinder where a large temperature gradient is induced. The Reynolds number and the Peclet number in this study are set to be 150 and 105. The values for α and N are 0.015 and 0.00494. The emissivity of the cylinder is set to be 0.7 while those of the inlet and outlet boundaries are 1.0.

The computational results for the direct problem are shown in Fig. 3(b)–(d) for the case when the temperature of cylinder surface is set to be 0.4. Fig. 3(b) depicts the stream line contours around the cylinder. The magnitude of maximum velocity is 2.352 at the mid point of the throat formed by two neighboring cylinders. A large recirculation region, the length of which is about 4.2, is formed behind the cylinder. Flow separation occurs at $\theta = 118.7°$. The temperature field is plotted in Fig. 3(c), exhibiting the isothermal lines clustered in the front region of the cylinder. The thermal boundary layer thickness in front of the cylinder is about 0.2. The temperature contour lines become wider downstream to the cylinder due to the flow separation, which results in a lower thermal conduction into the cylinder wall. The temperature averaged in the exit boundary is reduced to 0.812 due to the heat loss around the cylinder wall. Fig. 3(d) shows the divergence of the radiative heat flux vector. Negative divergence of radiative heat flux vector represents the thermal radiation absorbed by the local medium. The main radiative heat absorption is observed behind the cylinder. The contour lines are clustered just in front of the cylinder as in Fig. 3(c) for the temperature contour lines. Unlike the temperature contour, these contour lines can be found even in the far upstream of the cylinder because radiative heat transfer is effective even outside of the boundary layer.

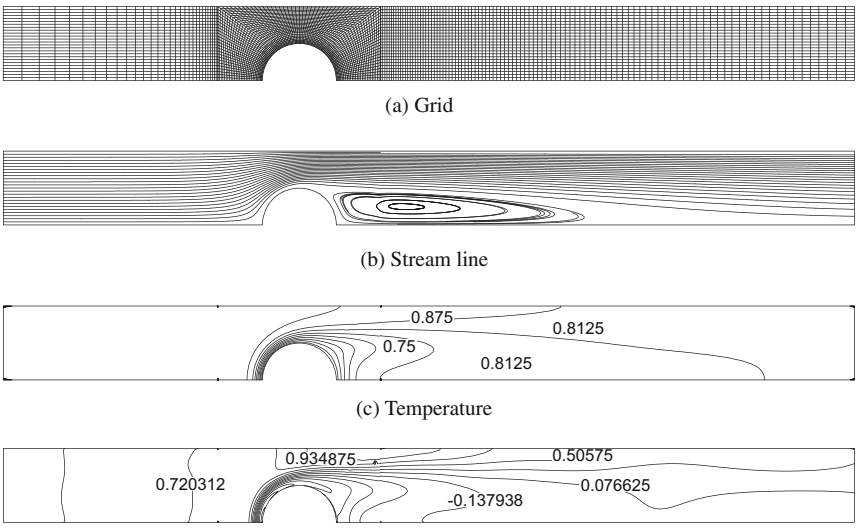

Fig. 3. Grid and results of direct problem.

4.2. Inverse problem calculation

In this section, the cylinder wall temperature is predicted by using the inverse technique, given the measured temperature data near the cylinder wall. The measured temperature data are obtained by adding some random errors to the calculated exact temperature data such that

$$Y_m = T_{exact} + \omega\sigma \tag{28}$$

where ω is a random variable with a range of $-2.576 \leqslant \omega \leqslant 2.576$, and σ is the standard deviation of the measurement errors.

The three types of cylinder wall temperature profiles are investigated in this study-constant, linear, and sinusoidal profiles.

$$F(\theta) = 0.4 \tag{29a}$$

$$F(\theta) = 0.4 + 0.15 \times \left(1 - \frac{\theta}{180}\right) \tag{29b}$$

$$F(\theta) = 0.4 + \frac{0.15}{2} \times (\cos(\theta\pi/180) + 1) \tag{29c}$$

Fig. 4 represents the effect of the measurement point location on the prediction for the constant profile given in Eq. (29a). In this case, there are no measurement errors in the medium temperature, i.e. $\sigma = 0.0$. A total of 23 measurement points (M = 23) are distributed along the half circle separated from the cylinder wall by the separation distance d. Three cases of the separation distance ($d_1 = 0.02$, $d_2 = 0.05$, and $d_3 = 0.09$) have been taken into account. If the separation distance is greater than the thermal boundary layer thickness, the cylinder wall temperature data can hardly reach the measurement points located upstream. Therefore, d is selected as lesser than the thermal boundary layer thickness. However, according to Fig. 4, the closer the measuring points are located to the cylinder, the larger the amplitude of fluctuation in the predicted wall temperature profiles. Although the predicted wall temperature profile for d_1 has the average value of 0.4, it can not be acceptable as a reasonable estimation due to a significantly oscillating temperature profile. The magnitude of oscillation for d_1 is almost equal to 0.1 of which the value is almost 10 times greater than the oscillation magnitude for d_2. The solution error for d_3 is almost negligible. The location of measurement points too close to the cylinder wall result in larger fluctuations in the predicted cylinder wall temperature profile, which is rather counter intuitive and requires additional explanation as below.

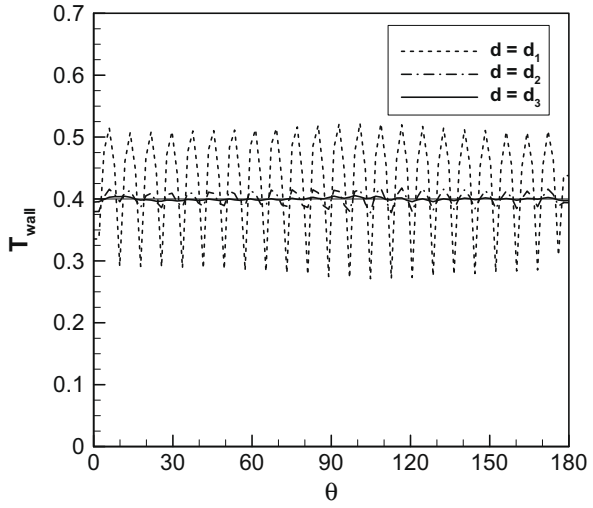

Fig. 4. Effect of measurement location on the constant temperature profile with $\sigma = 0.0$.

The contours of the Lagrange multiplier λ_T for the separation distance d_1 and d_3 at the 3rd iteration step are plotted in Fig. 5. It is clearly revealed that the contour line wiggles adjacent to the cylinder wall become stronger for a smaller separation distance. These wiggles are created by the action of source terms in Eq. (16). Such wiggles exert a disturbing effect on the gradient direction as defined in Eq. (19) which produce fluctuations in the predicted temperature profile. Consequently, the measurement points need to be located not too close to the cylinder, while not being located beyond the boundary layer, in order to obtain a sufficiently smooth solution.

Fig. 6 shows the effect of the number of measurement points on the prediction for the constant temperature profile. As in Fig. 6, the separation distance is fixed at d_3 for which the wiggles were found to be the smallest. Two cases of the measurement point number ($M = 12$ and $M = 23$) are tested. Relatively large fluctuations are observed for $M = 12$. On the other hand, when M is increased to 23, the fluctuations are adequately suppressed. The amplitude of fluctuation is observed to vary with θ. The largest amplitude for $M = 12$ occurs near $\theta = 120$, which appears to coincide with the flow sepa-

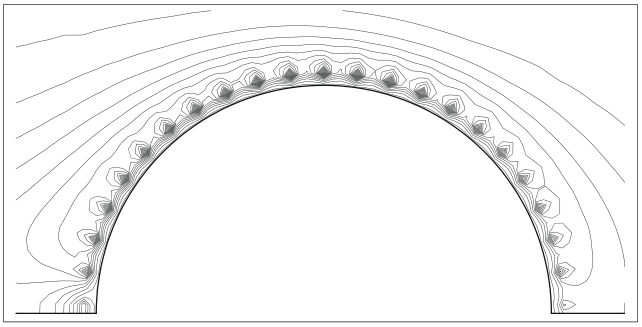

(a) d= d_1

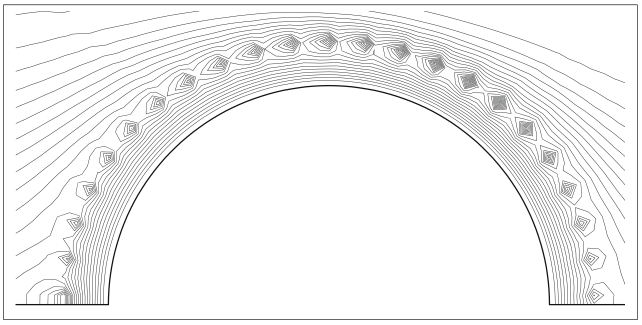

(b) d= d_3

Fig. 5. Contour plot of Lagrange multipliers λ_T at 3rd iteration step for $M = 23$.

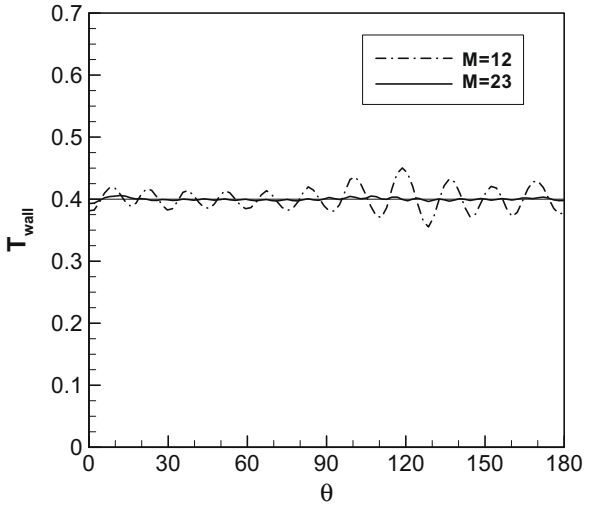

Fig. 6. Effect of the number of measurement points on the constant temperature profile with $\sigma = 0.0$.

ration angle. This simple test confirms that the prediction accuracy can be improved by increasing the number of measurement points. Nevertheless, an excessive number of measurement points would be impractical for actual measurements, therefore the number of measurement points should be chosen by optimizing the accuracy and the practicality.

Fig. 7 is a contour plot of λ_T for $M = 12$. The points A and C in the figure are chosen as two arbitrary neighboring measurement points projected into the cylinder wall. The point B is the middle point of A and C. The creation mechanism of fluctuations in the predicted profile is similar to that explained in the discussion for the effects of separation distance. That is, wiggles in λ_T contour line near the cylinder cause distortion in the gradient direction. However, the wiggles are produced not by a close proximity of measurement points to the cylinder wall but by an increased gap between neighboring measurement points in this case. It is believed that for $M = 12$, the two neighboring sources are not strong enough to disperse their information over the range covered by points A,B, and C. Especially, the intermediate measurement point B appears to receive less information from two neighboring measurement points than measurement point A or C. Although wiggles in λ_T contour line near the cylinder wall are not clearly seen in Fig. 7, fluctuations are clearly seen in the intermediate prediction profiles of Fig. 8.

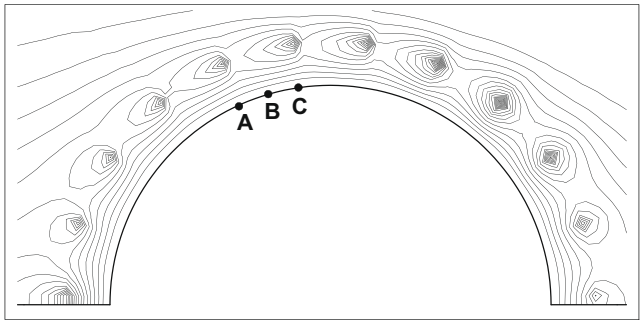

Fig. 7. Contour plot of Lagrange multipliers λ_T at 3rd iteration step for $M = 12$.

Fig. 9 show the effects of measurement error on the predicted profiles for various boundary temperature profiles. Two more measurement errors ($\sigma = 0.004$ and $\sigma = 0.008$) and two more boundary profiles (linear and sinusoidal) are taken into account. Based on the previous discussion, a total of 23 measurement points and location d_3 are chosen for this test. In case of $\sigma = 0.0$, prediction is well behaved for all the boundary profiles. On the other hand, when measurement data have some error, predicted profiles are somewhat deviated from the exact ones. It is expected that the larger the measurement error is, the greater the deviation of the predicted profile from the exact one is. The maximum error in the predicted profile for all the related boundary profiles is larger than the measurement error. The maximum deviation appears to be independent of the boundary profiles for the same measurement error, that is, 0.02 for $\sigma = 0.004$ and 0.03 for $\sigma = 0.008$.

5. Conclusion

The conjugate gradient method has been applied to predict the unknown surface temperature profiles of a cylinder, which is exposed to a hot gas flow. Conduction, convection, and radiation have

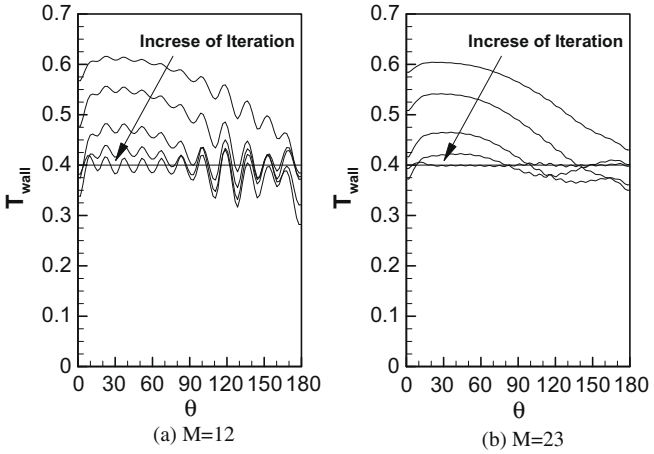

Fig. 8. Converging history with respect to iteration step with $\sigma = 0.0$.

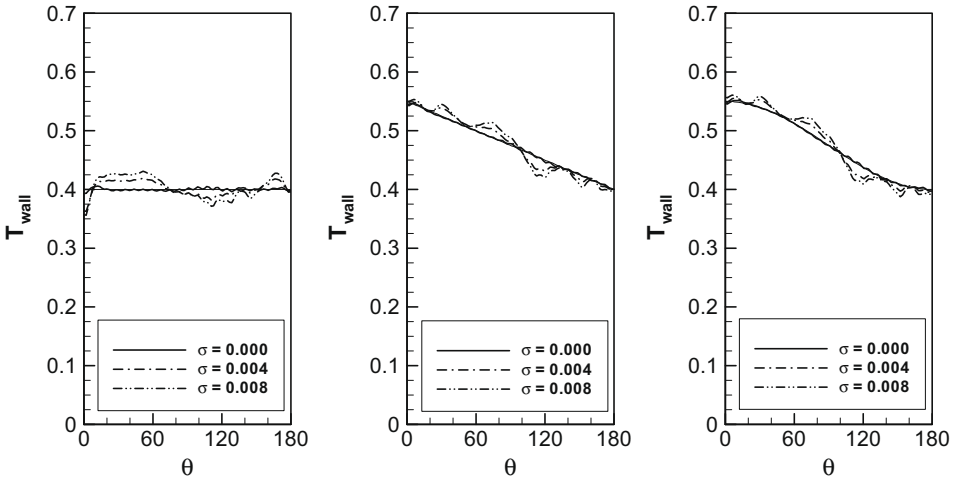

Fig. 9. Effect of measurement errors on the various temperature profiles.

been taken into account to calculate the heat transfer from the hot gas to the cylinder.

Amongst the three measurement locations ($d_1 = 0.02$, $d_2 = 0.05$, $d_3 = 0.09$), the location d_3 gives the most accurate prediction for the constant boundary temperature profile. When the measurement points are too close to the cylinder in case of d_1, large fluctuations are produced in the predicted profile. Locating measurement points closer to the cylinder wall results in stronger wiggles in the contour lines of Lagrange multiplies λ_T near the cylinder. Since these wiggles exert a disturbing effect on the gradient direction, fluctuations are produced in the predicted profiles.

When the number of measurement points is 12, relatively large fluctuations are also observed for the constant boundary temperature profile. The fluctuations are adequately suppressed by increasing the number of measurement points from 12 to 23. These results indicate that an appropriate number of measurement points is required to obtain a better estimation of the boundary temperature profile.

References

[1] W.M. Kays, A.L. London, Compact Heat Exchangers, McGraw-Hill, New York, 1984.
[2] A. Horvat, B. Mavko, Hierarchic modeling of heat transfer processes in heat exchangers, Int. J. Heat Mass Transfer 48 (2005) 361–371.
[3] M. Kawaji, X.H. Shen, H. Tran, S. Esaki, C. Dees, Prediction of heat transfer in the kraft recovery boiler superheater region, Tech. Assoc. Pulp Paper Ind. 78 (1995) 214–221.
[4] L.H. Liu, H.P. Tan, Q.Z. Yu, Simultaneous identification of temperature profile and wall emissivities in one-dimensional semitransparent medium by inverse radiation analysis, Num. Heat Transfer A 36 (1999) 11–525.
[5] H.Y. Li, Estimation of thermal properties in combined conduction and radiation, Int. J. Heat Mass Transfer 42 (1999) 565–572.
[6] H.K. Kim, A. Charette, A sensitivity function-based conjugate gradient method for optical tomography with the frequency-domain equation of radiative transfer, J. Quant. Spectrosc. Radiat. Transfer 104 (2007) 24–39.
[7] Y.K. Hong, S.W. Baek, Inverse analysis for estimating the unsteady inlet temperature distribution for two-phase laminar flow in a channel, Int. J. Heat Mass Transfer 49, 1137–1147.
[8] Y.K. Hong, S.W. Baek, Inverse heat transfer problem for natural convection with Radiation, in: 5th International Symposium on Radiative Transfer, 2007.
[9] I. Szczygiel, A. Fic, Inverse convection-diffusion problem of estimating boundary velocity based on internal temperature measurements, Inv. Probl. Eng. 10 (2002) 271–291.
[10] C.H. Huang, I.C. Yuan, H. Ay, A three-dimensional inverse problem in imaging the local heat transfer coefficients for plate finned-tube heat exchangers, Int. J. Heat Mass Transfer 46 (2003) 3629–3638.
[11] W.L. Chen, Y.C. Yang, An inverse problem in determining the heat transfer rate around two in line cylinders placed in a cross stream, Energy Conv. Manage. 48 (2007) 1996–2005.
[12] M.N. Özisik, R.B.O. Helcio, Inverse Heat Transfer, Taylor & Francis, New York, 2000.
[13] J.H. Ferziger, M. Peric, Computational Methods for Fluid Dynamics, Springer, 1996.
[14] B.G. Carlson, K.D. Lathrop, Transport Theory-the Method of Discrete Ordinates in Computing Methods in Reactor Physics, Gordon & Breach Science Publishers, New York, 1968.
[15] E.H. Chui, G.D. Raithby, Computation of radiant heat transfer on a nonorthogonal mesh using the finite-volume method, Num. Heat Transfer 23 (1993) 269–288.
[16] J.C. Chai, H.S. Lee, S.V. Patankar, Finite volume radiative heat transfer procedure for irregular geometries, AIAA J. Thermophys. Heat Transfer 9 (1995) 410–415.
[17] M.Y. Kim, S.W. Baek, Numerical analysis of conduction, convection, and radiation in a gradually expanding channel, Num. Heat Transfer 29 (1996) 725–740.